Journal of Solid State Electrochemistry
https://doi.org/10.1007/s10008-024-06011-4

ORIGINAL PAPER

# Modeling solid-state reaction processes: application for the archaeometric study of potteries from *Venus Fisica* Temple in Pompeii (Italy)

**Francesca Di Turo[1] · Caterina De Vito[2] · Fulvio Coletti[3] · Antonio Doménech-Carbó[4]**

Received: 5 March 2024 / Revised: 8 July 2024 / Accepted: 9 July 2024


## Abstract

This research employs the voltammetry of immobilized microparticles (VIMP) methodology to analyze a collection of ceramic samples from the temple of *Venus Fisica* in the archaeological site of Pompeii. The primary objective is to discern their origins and manufacturing processes by the solid-state analysis of the electroactive properties of iron minerals, particularly hematite, extensively investigated for its electrochemical and catalytic characteristics. In our study, we propose a model to elucidate the electrochemical processes involved, building upon prior logistic and nucleation formulations. In this model, we consider the possibility of two superimposed pathways. This approach provides a nuanced understanding of composition changes and mineral crystallinity, factors that can induce significant variations in the voltammetric signal. Consequently, it becomes an effective means to discriminate between different provenances and manufacturing techniques of different potteries. The outcomes of this research contribute valuable insights into the intricate realm of ancient ceramic materials, casting light on their origins and production processes within the historical context of Pompeii.

**Keywords** Ancient potteries · *Venus Fisica* Temple · Pompeii · Voltammetry of immobilized particles · Electrochemistry · Archaeometry

## Introduction

Ceramic materials hold significant importance in archaeology and archaeometry, possessing rich ethnohistorical value and widespread availability. However, their study presents challenges due to frequent recovery in fragmented states, with remains from different origins often overlapping. Therefore, analytical techniques for compositional and provenance studies become crucial for archaeological samples, especially in micro-invasive sampling.

Recently, the voltammetry of immobilized microparticles (VIMP) has proven effective in solving pivotal issues in discriminating unknown samples, being extensively used in cultural heritage studies [1–5]. To unravel the origins and manufacturing processes of a collection of 13 pottery samples originating from the *Venus Fisica* Temple in Pompeii, we have applied this technique. This approach allows for the extraction of chemical–mineralogical information from solid materials at the sub-microgram level [6–8]. Our ongoing research builds upon previous investigations into ceramic clay bodies [4, 5, 9–12], with a specific focus on the firing conditions employed in their production. This emphasis arises from the electroactive nature of iron minerals, particularly hematite, extensively studied for its electrochemistry and electro- and photoelectrocatalytic properties [13–18].

The extraction of archaeometric information requires the disposal of reasonable solid-state processes involved in the electrochemistry of iron minerals. In this context, the application of logistic [19] and nucleation-type [20] models was discussed to describe the solid-state redox processes accompanied by phase changes. More recently, these

✉ Francesca Di Turo
francesca.dituro@sns.it

✉ Antonio Doménech-Carbó
antonio.domenech@uv.es

[1] National Enterprise for nanoScience and nanoTechnology (NEST), Scuola Normale Superiore, Piazza dei Cavalieri, 7, 56126 Pisa, Italy

[2] Department of Earth Sciences, Sapienza University of Rome, P.le Aldo Moro 5, 00185 Rome, Italy

[3] Parco Archeologico del Colosseo - Ministero Della Cultura, Rome, Italy

[4] Departament de Química Analítica, Universitat de València, Dr. Moliner, 50, 46100 Burjassot, València, Spain

Published online: 22 July 2024

formulations were applied to ion-intercalation processes [21] with satisfactory results. Here, we extend these formulations to describe hematite-centered electrochemical processes considering the possibility of the coexistence of different pathways, a situation extensively treated in the modeling of ion-insertion electrochemistry [22, 23].

This study emerges as a pivotal tool for addressing crucial questions concerning the identification of pottery production centers in Pompeii, especially during the city's early periods. Our investigation delves into black-gloss ware and "bucchero" samples, aiming to discern whether the bucchero found in the archaic phase's stratigraphy or as residuals in the Hellenistic phase was a locally produced item or imported from Etruria or Lazio, as described in previous non-electrochemical studies [24–33].

The current article advances beyond the existing state of the art by showcasing the fundamental significance of applying electrochemical techniques and a thorough comprehension of solid-state processes in the field of archaeometry. Our objective is to enhance the broader understanding of Pompeii's ceramic production landscape, leveraging the electroactive characteristics of iron minerals.

## Experimental

### Materials

Our analyses center on thirteen fragments, addressing crucial questions for identifying the production centers of pottery circulating in Pompeii, particularly during the city's earliest periods. We aim to determine whether the bucchero found in the stratigraphies of the archaic period or as residuals in the Hellenistic phases was a local product or imported from Etruria or Lazio (Italy).

Additionally, our investigation extends to understanding to what extent the production of black-painted ceramics from the Gulf of Neapolis differs from that manufactured in Pompeii. Information regarding the samples analyzed here is given in Table 1. The archaeological context and petrographic analyses conducted previously can be found in the supplementary material.

As regards Pompeian production, jug and a patera fragments of bucchero were analyzed (respectively Nrr. Inv. 4226.109, 4020.107). The bottom of a skyphos with painted traces (Nr. Inv. 4032.105), a patera (Inv. Nr. 4032.104) in BGW, and two cups in BGW (Inv. Nr. 4226.108 and 4226.110) were analyzed. Other two cup samples, classified as common pottery and Pre-sigillata (Nr. Inv.1_403_405 and 4032_Tav XV_9), were analyzed. Finally, a brown unidentified fragment (Nr. Inv.14226_106) is investigated.

About Apulian production, a unit belonging to a kỳlix has been identified (Inv. Nr. 4032.103), while to the manufacturers of southern Etruria, perhaps at the port of Pirgy, fragments of the edge of a patera (Inv. Nr. 4032.101). Finally, a kylix and a patera belong to the area of southern Lazio, perhaps to the production of Minturno (Nrr. Inv. 4226.102 and 4032.158) [27–31]. It is pertinent to note that crystallization of hematite starts above 600 at the expense of Fe-hydroxide forms during firing in an oxidizing atmosphere according to the reaction: $2\alpha\text{-FeO(OH)} \rightarrow \alpha\text{-Fe}_2\text{O}_3 + \text{H}_2\text{O}$. Then, hematite is a ubiquitous but a minority component that influences the color significantly [24–32].

### Instrumentation and methods

Voltammetry measurements were performed using CH 720c equipment (Cambria Scientific, Llwynhendy, Llanelli UK). The voltammetry of sample-modified graphite electrodes was studied at room temperature ($298 \pm 1$ K) in a

**Table 1** Main characteristics of samples in this study

| Sample | Color | Type | | Attributed provenance |
|---|---|---|---|---|
| 4032_158 | Brown | Kylix and a patera | BGW | Southern Lazio, perhaps to the production of Minturno |
| 4226_109 | Black | A jug and a patera | Bucchero | Pompeii workshop |
| 4032_103 | Brown | Kylix and a patera | BGW | Apulian |
| 4226_110 | Black | Cup | Bucchero | Pompeii workshop |
| 4026_102 | Brown | Kylix and a patera | BGW | Southern Lazio, perhaps to the production of Minturno |
| 4032_101 | Brown | Edge of a patera or plate | BGW with iridescence | Etruria, perhaps at the port of Pirgy |
| 4226_106 | Brown | Unidentified | BGW with iridescence | Pompeii workshop |
| 4226_108 | Black | Cup | Bucchero | Pompeii workshop |
| 1_403_405 | Brown | Cup | Common pottery | Pompeii workshop |
| 4032_Tav XV_9 | Red | Cup | Pre-sigillata | Pompeii workshop |
| 4020_107 | Grey | A jug and a patera in bucchero | Bucchero | Pompeii workshop |
| 4032_105 | Brown | Skyphos with painted traces | BGW | Pompeii workshop |
| 4032_104 | Brown | Patera | BGW | Pompeii workshop |

conventional three-electrode cell including a platinum disc auxiliary electrode and an Ag/AgCl (3 M NaCl) reference electrode. Air-saturated 1.0 M $H_2SO_4$ and 0.25 M HAc/NaAc (pH 4.75) aqueous solutions were used as electrolyte solutions. Commercial graphite bars (Alpino Maxim HB-type, 2 mm diameter) were used as working electrodes, completing the three-electrode arrangement with a platinum disc auxiliary electrode and an Ag/AgCl (3 M NaCl) reference electrode. Electrode modification was carried out by scratching ca. 1 µg of solid material from the cross-section of the ceramic fragments with the help of a scalpel. The resulting ceramic powder was extended, forming a fine coating on one plane face of an agate mortar. Subsequently, portions of this powder were transferred to the graphite electrode using an abrasion technique. This method involves rubbing or scraping the ceramic powder onto the surface of the graphite electrode, likely to achieve a specific coverage or distribution. Square wave voltammetry was used as the detection mode. To avoid possible biased selection of samples, these were randomized before voltammetric experiments.

## Results and discussion

### General voltammetric response

Figure 1 shows the cyclic voltammogram of sample 4032_101: in the initial anodic scan, a well-defined oxidation peak (A) appears at ca. 0.95 V vs. Ag/AgCl. This process is irreversible, and it is preceded by a shoulder near 0.70 V (marked by a dotted arrow in the figure). In the subsequent cathodic scan, reduction peaks at 0.3 (G), − 0.2 (B), and − 0.7 V (C) appear. The former is coupled with an oxidation counterpart at 0.40 V corresponding, according to previous studies [11, 12, 33, 34], to a redox process involving oxygen functionalities in the graphite surface. In turn, process B can be assigned to the proton-assisted reduction of Fe(III) minerals, and process C corresponds to the reduction of dissolved oxygen (oxygen reduction reaction, ORR) catalyzed by crystalline hematite superimposed to the reductive dissolution of this compound [12, 14–18, 35]. It should be noted that the voltammetric response of solid materials depends not only on the chemical/mineralogical composition but also on the shape and size distribution of the solid particles. Under our experimental conditions, these factors influence more significantly the impedance response than the voltammetric one [11, 23, 34].

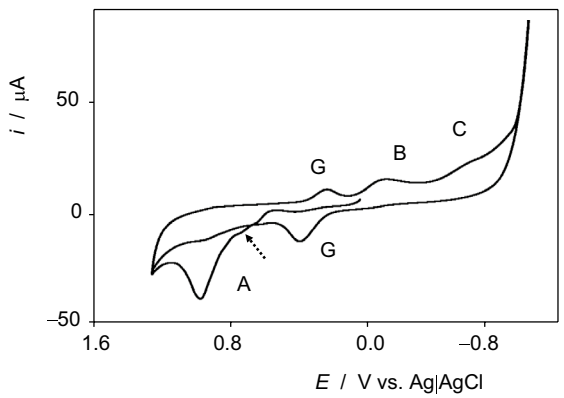


**Fig. 1** Cyclic voltammogram of sample 4032_101 attached to graphite electrode in contact with air-saturated 1.0 M $H_2SO_4$. Potential scan initiated at 0.0 V vs. Ag/AgCl in the positive direction, potential scan rate 50 mV $s^{-1}$. The weak shoulder at ca. 0.70 V is marked by a dotted arrow

Depending on the electrochemical conditions, the reduction of hematite results in the formation of $Fe^{2+}$(aq) plus Fe(III)Fe(II) hydroxylated hematite. These processes can be represented as follows:

$$Fe^{III}{}_2O_3 + 6H^+(aq) + 2e^- \rightarrow Fe^{2+}(aq) + 3H_2O \quad (1)$$

$$Fe_2O_3 + xH^+(aq) + xe^- \rightarrow Fe^{III}{}_{2-x}Fe^{II}{}_xO_{3-x}(OH)_x \quad (2)$$

Hematite acts catalytically on the ORR process (D), either chemically [14, 15] or electrochemically [12, 23]. The same effect is, in principle, produced by Fe(II) minerals existing in the solid sample [5], resulting in an increase of the peak current C at sample-modified electrodes relative to that current measured at unmodified graphite electrodes. In the region of positive potentials, peak A can be attributed to the oxidation of hematite to hydroxylated forms in higher iron oxidation states [33–37]. This process can be represented as [38]

$$Fe^{III}{}_2O_3 + 2xH_2O \rightarrow Fe^{IV}{}_xFe^{III}{}_{2-x}O_3(OH)_{2x} + 2xH^+(aq) + 2xe^- \quad (3)$$

For our purposes, the key point to emphasize is that the voltammetric response is sensitive to the composition and textural properties (crystallinity, porosity, hardness, compactness, etc.) of the solid sample. These properties, in turn, depend on the composition of the raw material and the manufacturing process. Ultimately, the voltammetric response will be sensitive to the firing temperature: above 500–900 °C, hematite becomes dehydroxylated, and since crystalline hematite is a more efficient catalyst than its hydroxylated forms, the intensity of the ORR signal will be sensitive to the firing temperature. This signal can also be influenced by the catalytic effect of Fe(II) minerals [39], whose proportion in ceramic pastes significantly increases when the firing process is carried out under reducing conditions.

## Modeling

The processes described by Eqs. (1)–(3) can be treated, in principle, assuming that ion insertion plays an essential role in the overall electrochemical process. In the classical formulation from Levi and Aurbach [34, 35], the advance of the process can be represented by the Langmuir isotherm

$$\frac{1-x}{x} = \exp\left[\frac{nF(E-E^{\circ})}{RT}\right] \tag{4}$$

Here, $x$ is the intercalation level, and $E$ is the potential applied to the working electrode. $x$ corresponds to the ratio between the net number of intercalated ions and the total number of intercalation sites. This quantity can be seen as the ratio between the charge passed $q$ and the maximum charge to be passed during a voltammetric experiment, $q_o$.

The current $i$ measured in a voltammetric experiment under quasi-equilibrium conditions can be expressed as the product of potential scan rate by a term similar to the pseudo-capacity characterizing surface-confined electrochemical processes [34, 35]

$$i = v\frac{dx}{dE} \tag{5}$$

The Langmuir isotherm can be reproduced simply assuming that the $dx/dE$ function corresponds to a logistic growth of type [19]

$$\frac{dx}{dE} = kx(1-x) \tag{6}$$

where $k$ represents a rate constant. Accordingly, linear potential scan voltammograms can be described by the equation

$$i = q_o kv\frac{e^{k(E-E^{\circ})}}{\left[1+e^{k(E-E^{\circ})}\right]^2} \tag{7}$$

This expression applies to reversible ion-intercalation processes under quasi-equilibrium conditions. Deviations from reversibility in the electron transfer and geometric constraints involved in the intercalation process can be modeled either by introducing other logistic-type equations [19, 20] or by introducing nucleation equations of the type [20]. In the first approach, the Richards equation [36],

$$\frac{dx}{dE} = kx(1-x^{\gamma}) \tag{8}$$

leads to current/potential curves of the type

$$i = q_o kv\frac{e^{k(E-E^{\circ})}}{\left[1+e^{\gamma k(E-E^{\circ})}\right]^{\frac{1}{\gamma}+1}} \tag{9}$$

The second approach gives

$$-[\ln(1-x)]^{1/m} = G(E-E_i) \quad ; \quad |E| > |E_i| \tag{10}$$

Here, $E_i$ represents the initial potential of the voltammogram, and the exponent $m$ is representative of the dimensionality of the nucleation process. In the classical Avrami kinetics, $m$ can take the values $m=2, 3, 4$. Fractional $m$ values can be taken eventually and seen as representative of the fractal dimension of the nucleation. Now, the voltametric current/potential curve is represented by the equation

$$i = vq_o\left[G^m(E-E_i)^{m-1}\exp\left[-G(E-E_i)\right]^m\right] \tag{11}$$

However, many systems show more complex growth pattern, characterized by the occurrence of multiple processes sequentially or simultaneously [37]. Let us consider a system growing in two discrete phases, termed as bi-logistic [38, 39]. In principle, the system growth can be expressed as the sum of two components

$$x(t) = x_1(t) + x_2(t) \tag{12}$$

where $x_1(t)$ and $x_2(t)$ are the populations at time $t$ of the phases 1 and 2.

The first description of this kind of systems was proposed independently by Lotka [37] and Volterra [40, 41] in the 1920s. This can be represented by the differential equation [42]

$$\frac{dx_1(t)}{dt} = k_1x_1(t)\left[1-\frac{x_1(t)}{x_{1\lim}}+p_{12}\frac{x_2(t)}{x_{1\,\lim}}\right] \tag{13}$$

where $k_1$ is the exponential rate of growth of the first species when both the 1 and 2 population densities are low; $x_{1\lim}$ is the carrying capacity of species 1 in the absence the species 2, and $p_{12}$ is the linear reduction of the growth rate of the species 1 by its competitor, the species 2.

Assuming that the two phases grow independently following a logistic pattern, the aggregate $x(t)$ vs. $t$ curve can offer different appearances [33]. In the case of "sequential" or "paused" growth, the second process does not start growing until the first pulse has nearly reached its saturation level. Then, the global curve shows two consecutive s-shaped regions. If the second process starts when the first phase has reached a significant (ca. 50% saturation) level of development, the two s-shaped waves merge. This situation occurs for systems growing via two concurrent processes of a similar nature. When the first process is joined by the second, faster process, a unique s-shape curve is obtained. This is the converging case, roughly equivalent in appearance to the diverging one. Here, the two processes initiate at the same time but grow with different rates and carrying capacities [33].

We can apply this general view to describe the well-defined signal A in the voltammetric records such as in

Fig. 1. In principle, the two-wave pattern can be approximated by a paused growth involving two intercalation pathways

$$i = q_{o1} g v \frac{e^{g(E-E_1)}}{\left[1 + e^{\gamma g(E-E_2)}\right]^{\frac{1}{\gamma}+1}} + q_{o2} h v \frac{e^{h(E-E_2)}}{\left[1 + e^{\lambda h(E-E2)}\right]^{\frac{1}{\lambda}+1}} \quad (14)$$

each one a function of its respective rate constant ($g$, $h$), formal electrode potential ($E^{\circ}_1$, $E^{\circ}_2$), saturation charge ($q_{o1}$, $q_{o2}$), and exponent ($\gamma$, $\lambda$). In turn, for two Avrami-type patterns,

$$i = v q_{o1} \left[G^m (E - E_i)^{m-1} \exp\left[-G(E - E_i)\right]^m\right] + v q_{o2} \left[H^r (E - E_i)^{r-1} \exp\left[-H(E - E_i)\right]^r\right] \quad (15)$$

Now, two different charge saturations ($q_{o1}$, $q_{o2}$) and two different exponents ($m$, $r$) are introduced. However, it is possible to conceive a third situation where one pathway replaces the other. Qualitatively, the change in the electrochemical mechanism is consistent with the aforementioned approaches to intercalation reactions [22, 23, 39] and the description of such processes from Malaie et al. [43, 44].

We focus our attention on the anodic signal A which exhibits a peak preceded by a weak shoulder. The best fit of experimental data can be obtained assuming that the oxidation process initially follows a nucleation mechanism that becomes further superimposed to a logistic growth. Figure 2a shows the experimental data for signal A recorded for sample 4032_101 superimposed to the theoretical current/potential curves predicted from Eq. (11) taking $G = 0.0025$ mV$^{-1}$, $q_o v G^m = 10.0$ μA, and $m = 2$ (squares), and Eq. (10) inserting $E^{\circ\prime} = 0.90$ V, $q_o k v = 34$ μA, $\gamma = 0.60$, $k = 20$ V$^{-1}$ (circles). The sum of the two theoretical curves (continuous line in Fig. 2) is coincident with experimental data.

For our purposes, the relevant point to emphasize is that the different ceramic samples, although displaying qualitatively similar voltammetric patterns, exhibit subtle but consistent differences in the voltammetric parameters. This can be seen by comparing the data for peak A for samples 4032_101 (Fig. 2a) and 4020_107 (Fig. 2b). In this second case, experimental data can be reproduced from Eq. (11) taking $G = 0.0020$ mV$^{-1}$, $q_o v G^m = 7.5$ μA, and $m = 2$, and Eq. (10) inserting $E^{\circ\prime} = 0.90$ V, $q_o k v = 32$ μA, $\gamma = 0.65$, $k = 15$ V$^{-1}$ (circles). These features support the idea that voltammetric data can detect regularities in the properties of ceramic specimens.

## Screening

For screening purposes, square wave voltammetry offers a sensitive method to group/discriminate different sets of samples [4, 5, 11, 12]. Figure 3 depicts the square wave voltammograms recorded for sample 4032_101. While scanning the potential

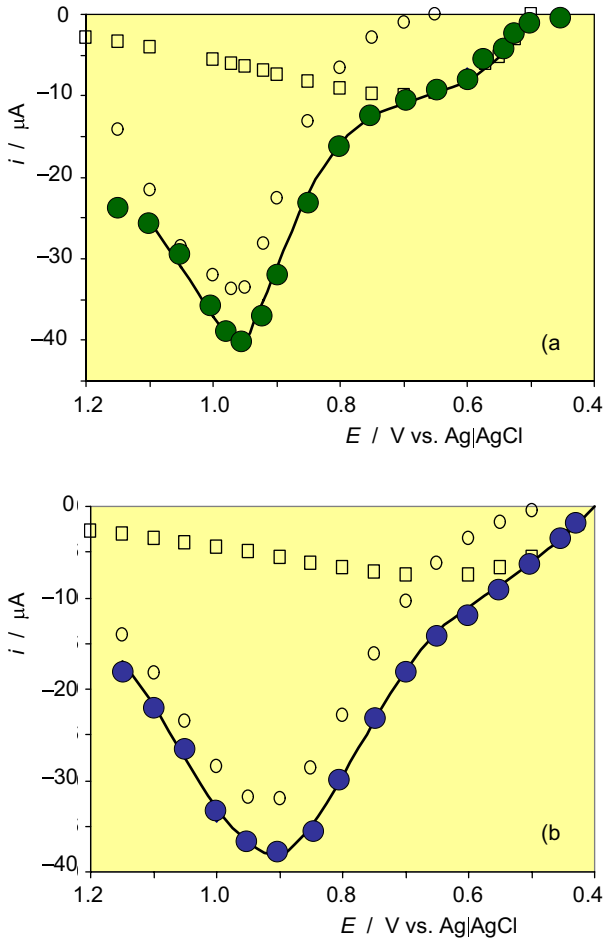


**Fig. 2** Experimental current/potential curves for signal A (solid circles) for samples **a** 4032_101 and **b** 4020_107. Theoretical waves predicted from Eqs. (10) and (11), taking: **a** $G = 0.0025$ mV$^{-1}$, $q_o v G^m = 10.0$ μA, and $m = 2$ (squares), $E^{\circ\prime} = 0.90$ V, $q_o k v = 33.6$ μA, $\gamma = 0.60$, $k = 20$ V$^{-1}$ (circles); **b** $G = 0.0020$ mV$^{-1}$, $q_o v G^m = 7.5$ μA, and $m = 2$ (squares), $E^{\circ\prime} = 0.90$ V, $q_o k v = 32.0$ μA, $\gamma = 0.65$, $k = 15$ V$^{-1}$ (circles). The continuous line corresponds to the sum of the theoretical curves from Eqs. (10) and (11) in each case

from 1.25 V vs. Ag/AgCl in the negative direction, the voltammograms in acetate buffer (Fig. 1a) exhibit an intense initial current corresponding to the oxygen evolution reaction (OER). Subsequently, a peak at approximately 1.0 V (A) is followed by a second signal around − 0.1 V (B) and a more prominent peak at about − 1.0 V (C). This signal is succeeded, at extreme negative potentials, by a rising current corresponding to the hydrogen evolution reaction (HER). This current is enhanced relative to unmodified graphite electrodes, thus suggesting that the ceramic materials exert a moderate catalytic effect on the HER process. The voltammograms in contact with 1.0 M $H_2SO_4$ solution (Fig. 1b) display a similar pattern, now incorporating a sharp peak at about 0.3 V (G). In the region of potentials between 0.0 and around − 1.2 V, signal C is replaced by peaks at approximately − 0.7 V (D) and − 1.0 V (E).

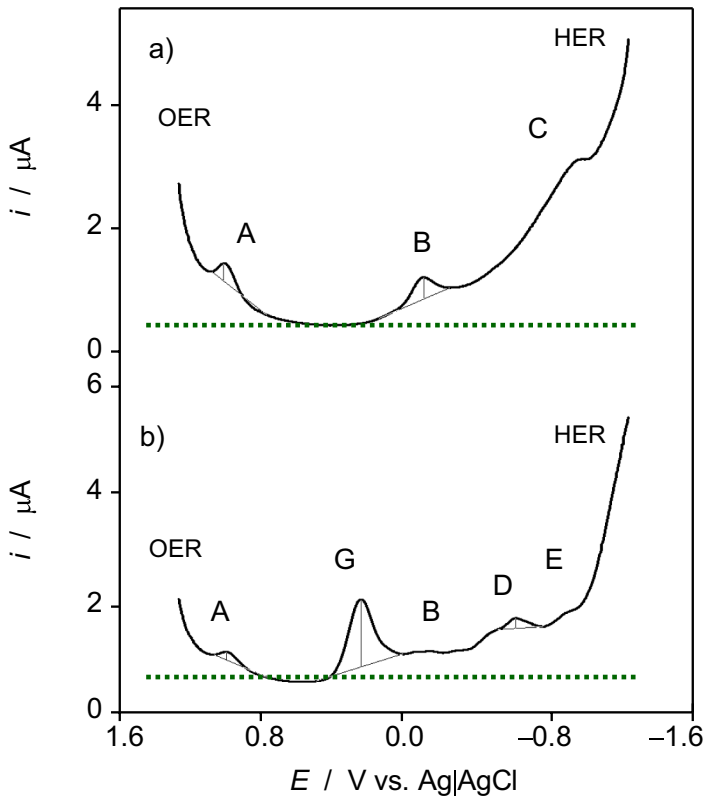


**Fig. 3** Square wave voltammograms of microparticulate deposits from sample 4032_101 attached to graphite electrode in contact with air-saturated **a** 0.25 M HAc/NaAc, pH 4.75, and **b** 1.0 M $H_2SO_4$ aqueous solutions. Potential scan initiated at 1.25 V vs. Ag/AgCl in the negative direction; potential step increment 4 mV; square wave amplitude 25 mV; frequency 10 Hz. The dotted lines mark the baselines used to measure peak currents

To discriminate between different ceramic samples, it is worth noting that the voltammetric response of iron minerals, as well as their catalytic effect on electrochemical processes such as ORR, HER, and OER, will depend on the composition, crystallinity, and degree of hydration of the minerals. The electrocatalysis of hematite in the OER reaction has been widely studied in the context of semiconductor electrochemistry [13, 45–49]. The proposed mechanism involves hole generation and the oxidation of deprotonated surface hydroxyls coupled to Fe(III)/Fe(IV) transformations; the rate-determining step involves the formation of an O – O bridge between contiguous oxygen atoms bound to surface iron centers [48].

As previously noted, the effect of hematite on the ORR process has been described by Shimizu et al. [15, 16] in terms of the catalytic promotion of the disproportionation of $H_2O_2$, the primary product of the electrochemical reduction of $O_2$, into $H_2O$ and $O_2$. In addition to the above "chemical" mechanism, we proposed an "electrochemical" one involving the reaction with $O_2$ of iron active sites generated in the process described by Eq. (16) [12, 33]. This reaction, which accelerates the initial step of the ORR process, yields superoxide radical anion, $O_2^{-}$, as

$$\mathrm{Fe^{III}}_{2-x}\mathrm{Fe^{II}}_{x}\mathrm{O}_{3-x}(\mathrm{OH})_x + x\mathrm{H_2O} + \mathrm{O_2} \rightarrow \mathrm{Fe^{III}}_{2}\mathrm{O}_{3-x}(\mathrm{OH})_{2x} + x\mathrm{H^{+}}_{\mathrm{aq}} + \mathrm{O_2}\cdot^{-} \quad (16)$$

The produced superoxide radical anion can then experience the subsequent chemical/electrochemical steps yielding $H_2O_2$ and $H_2O$. This is consistent with the results reported by Wan et al. [18] on the activation of the electrocatalytic activity of hematite nanoparticles via its reduction so that the major catalytic performance was achieved for magnetite ($Fe_3O_4$) plus hematite composites.

Electrocatalytic effects on HER have been described for several molecular Fe(II) catalysts such as tetradentate phosphine ligands, clathrochelates, and porphyrins [49–52]. The catalytic cycle has been described in terms of an initial one-electron reduction to Fe(I), that is the catalytically active species. This is protonated to form an iron-hydride complex which subsequently reacts with hydrogenions yielding $H_2$ and a Fe(III) complex which is electrochemically reduced to the parent Fe(II) complex [33–35]. In the case of Fe(III) and Fe(II) minerals, whose electrochemical reduction takes place at potentials similar to those where the HER process occurs, it is conceivable that any equivalent catalytic scheme could be operative via the generation of coordinatively unsaturated Fe(II) and Fe(I) centers.

As is customary in VIMP experiments, one can assume that the intensity of the voltammetric signals depends on the net amount of the respective electroactive species [1–4]. Then, as far as the net amount of sample transferred onto the

electrode cannot be accurately controlled, the absolute intensities vary for replicate experiments on the same sample. In addition, there are deviations from linearity in the intensity/sample amount as a result of the variations in the effective contact between the solid particles and the graphite active sites [3]. Accordingly, we will analyze experimental voltammetric data in terms of tendency graphs of different pairs of intensities ($i$(J)). These were measured using the baselines depicted in Fig. 3.

First of all, we compare local Pompeii productions distinguishing between "brown" samples and "grey" samples. Figure 4 shows the $i$(OER) vs. $i$(B) and $i$(HER) vs. $i$(B) representations for such samples in contact with acetate buffer. Here, we have adopted the signal at − 0.1 V (B) as a reference because it is confined to a narrow range of absolute values in all cases. One can see in this figure that both the signal A and the HER current are more intense for "grey" than for "brown" Pompeii samples.

Confirming the above peak assignments, we obtain that the intensity of the HER process is strongly correlated with the intensity of the overlapping reduction processes labeled as C measured in acetate buffer. Both "grey" and "red" data points fall in the (essentially) common tendency (almost) straight line passing by the origin, as can be seen in Fig. 5. Remarkably, plots of $i$(HER) vs. $i$(OER) discriminate not only between "brown" and "grey" samples produced in the Pompeii workshops but also between samples 4020_107 and samples 4226_108, 4226_109, and 4226_110. The former is a grey jug and a patera in bucchero, whereas the other three samples, which exhibit a homogeneous response, correspond to black cups (4226_108 and 4226_110) and a second patera in bucchero (4226_109). This can be seen in Fig. 6, where the different sets of samples are grouped on tendency potential lines.

Roughly, this diagram can be seen as representative of two parameters associated with the firing process: the firing temperature and the reducing/oxidizing conditions of firing. In principle, the intensity of the OER signal should increase on increasing the crystallinity of the catalytic iron species [33, 34] so that a larger $i$(OER) denotes larger firing temperatures. In turn, the intensity $i$(HER) should increase on increasing the proportion of Fe(II) species, *i.e.*, on increasing the reducing conditions of firing.

These apparent tendencies are represented by arrows in Fig. 4. However, it has to be taken into account that different factors are superimposed, often contradictorily, in the above general trends. For instance, the crystallinity of mineral components should favor all (OER, HER, ORR) catalytic processes. Other factors, namely, the heterogeneity of the shape and size particle distribution or the proportion of hard minerals such as quartz can influence the voltammetric response [23, 34].

Keeping in mind these considerations, voltammetric data can discriminate both the provenance and manufacturing techniques. This can be seen in Fig. 7, where "brown" samples in this study are grouped based on plots of $i$(C) vs.

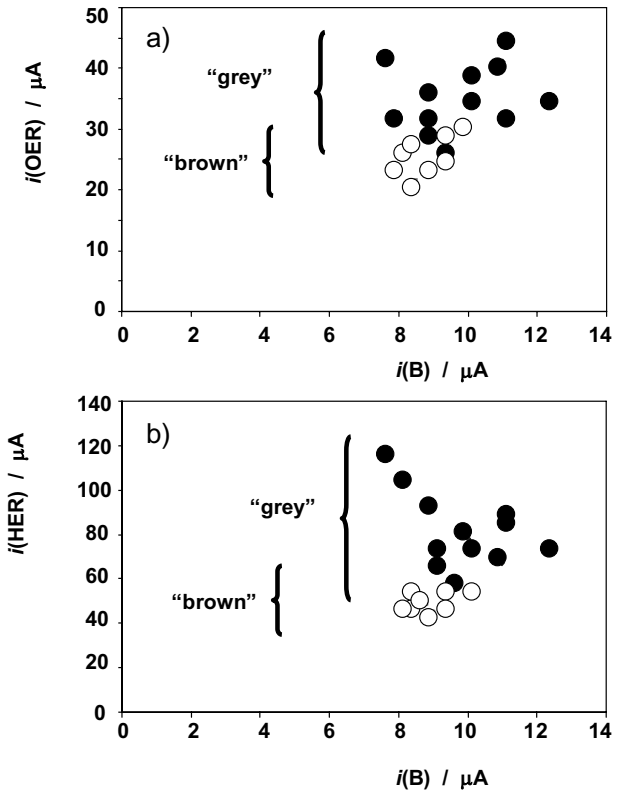


**Fig. 4** Plots of **a** $i$(OER) vs. $i$(B) and **b** $i$(HER) vs. $i$(B) for voltammetric data of the studied samples from Pompeii local productions in contact with aqueous acetate buffer at pH 4.75. "grey" (solid circles) and "brown" (circles) samples are separately plotted. Three independent measurements for each sample are represented

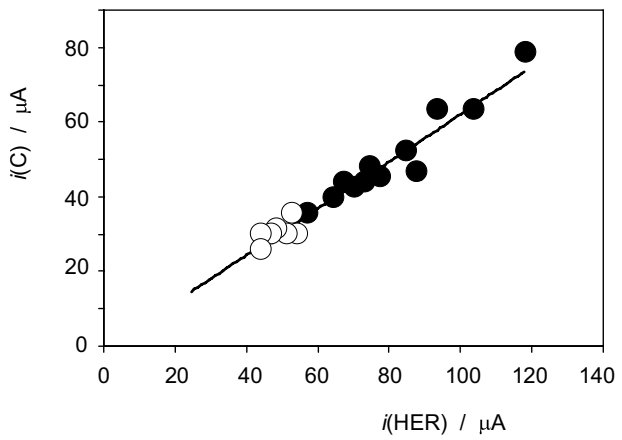


**Fig. 5** Plots of $i$(C) vs. $i$(HER) for voltammetric data of the studied samples from Pompeii local productions in contact with aqueous acetate buffer at pH 4.75. "Grey" (solid circles) and "brown" (circles) samples are separately plotted. Three independent measurements for each sample are represented

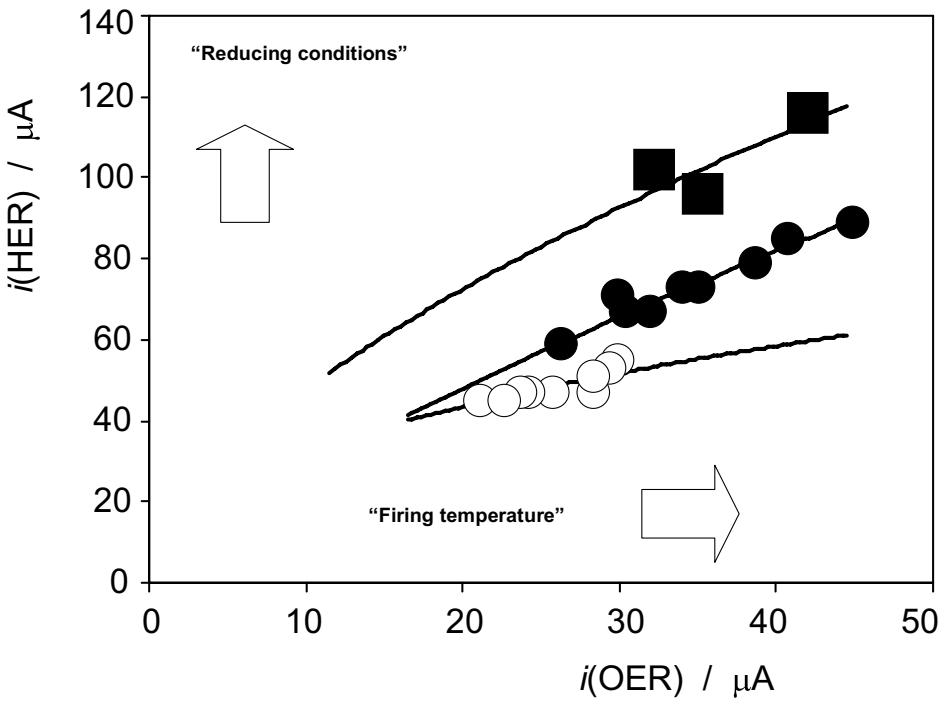


**Fig. 6** Plots of *i*(HER) vs. *i*(OER) for voltammetric data of the studied samples from Pompeii local productions in contact with aqueous acetate buffer at pH 4.75. "Grey" samples 4226_108, 4226_109, 4226_110 (solid circles) and 4020_107 (squares) and "brown" (circles) samples are separately plotted. Three independent measurements for each sample are represented

*i*(OER). Experimental data points can be separated into four tendency lines. The Pompeii productions are separated into two trend lines, by the one hand, samples 4226_106 and 1_403_405 (circles), two brown fragments of unidentified objects, and by the second hand, sample 4032_Tav XV_9, (triangles) corresponding to a red object. These samples are separated from the Apulian sample 4032_103 (solid triangles). Samples from Etruria (4032_101) and Lazio (4026_102, and 4032_158) workshops (solid triangles) become unified in a common tendency line.

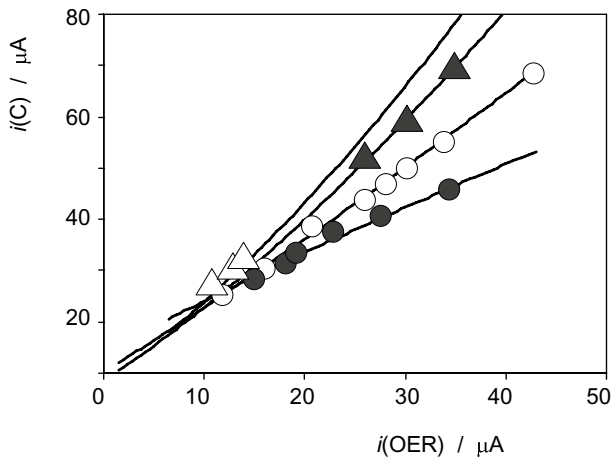


**Fig. 7** Plots of *i*(C) vs. *i*(OER) for voltammetric data of the "brown" samples in this study in contact with aqueous acetate buffer at pH 4.75. Solid circles: Pompeii samples 4226_106 and 1_403_405; circles: samples 4032_101, 4026_102, and 4032_158 (Etruria and Lazio workshops); solid triangles: Apulian sample 4032_103; triangles: 4032_Tav XV_9 from Pompeii workshop. Continuous lines correspond to the fit of experimental data to potential functions

## Conclusions

The voltammetric response of clay ceramics in contact with air-saturated aqueous electrolytes consists of different oxidation and reduction processes associated with iron (mainly hematite) minerals accompanied by catalytic effects on hydrogen evolution, oxygen evolution, and oxygen reduction reactions. The voltammetric response can be modeled satisfactorily using logistic- and Avrami-type approaches. These approaches reveal that subtle changes in the composition, crystallinity, etc. of the minerals can produce significant variations in the voltammetric pattern. This confirms the sensitivity of the solid-state voltammetry to changes in the manufacturing type (granulometry, firing conditions, etc.) and, consequently, the suitability of voltammetric data to discriminate between different ceramic productions.

**Supplementary Information** The online version contains supplementary material available at https://doi.org/10.1007/s10008-024-06011-4.

**Funding** Open access funding provided by Scuola Normale Superiore within the CRUI-CARE Agreement. The work was carried out within the framework of project PID2020-113022 GB-I00 which was financially supported by*Ministerio de Ciencia e InnovaciónandAgencia*

*Estatal de Investigación(AEI) of the Spanish government. This research was also funded by Sapienza University of Rome, a grant in 2021.*



## References

1. Doménech-Carbó A (2010) Voltammetric methods applied to identification, speciation, and quantification of analytes from works of art: an overview. J Solid State Electrochem 14:363–379
2. Doménech-Carbò A, Doménech-Carbò MT (2023) Electrochemistry for cultural heritage, monograph in electrochemistry, Scholz, F. Peter, L. Eds. Gualaboski R and Mirceski V, Springer 28:1417–1420
3. Doménech-Carbó A, Scholz F (2019) Electrochemical age determinations of metallic specimens - utilization of the corrosion clock. Acc Chem Res 52:400–406
4. Di Turo F, Montoya N, Piquero-Cilla J et al (2018) Electrochemical discrimination of manufacturing types of pottery from Magna Mater Temple and Fora of Nerva and Caesar (Rome, Italy). Appl Clay Sci 162:305–310
5. La-Torre-Riveros L, Doménech-Carbó A, Cabrera CR, Doménech-Carbó MT, Huahuasoncco-Condori W, Guzmán DQ, Gutiérrez-Castillo MC, Carmona-Ochoa K, Pérez-Trujillo A (2019) Solid-state electrochemical analysis of Inka pottery from Qotakalli archeological site in the Cusco (Perú) area. J Solid State Electrochem 23:1541–1552
6. Scholz F, Meyer B (1996) Voltammetry of solid microparticles immobilized on electrode surfaces. Electroanal Chem 20:1–82
7. Scholz F, Schröder U, Gulaboski R, Doménech-Carbó A (2015) Electrochemistry of immobilized particles and droplets. Monographs in Electrochemistry series, Experiment with three-phase electrodes. Scholz F, Ed. Springer Cham, Berlin-Heidelberg, pp-XV-327. https://doi.org/10.1007/978-3-319-10843-8
8. Doménech-Carbó A, Labuda J, Scholz F (2013) Electroanalytical chemistry for the analysis of solids: characterization and classification (IUPAC Technical Report)*. Pure Appl Chem 85:609–631
9. Doménech-Carbó A, Sánchez-Ramosa S, Doménech-Carbó MT, Gimeno-Adelantado JV, Bosch-Reig F, Yusá-Marco DJ, Saurí-Peris MC (2002) Electrochemical determination of the Fe(III)/Fe(II) ratio in archaeological ceramic materials using carbon paste and composite electrodes. Electroanalysis 14:685–696
10. Sánchez Ramos S, Bosch Reig F, Gimeno Adelantado J, Yusá-Marco DJ, Doménech-Carbó A (2002) Application of XRF, XRD, thermal analysis, and voltammetric techniques to the study of ancient ceramics. Anal Bioanal Chem 373:893–900
11. Fabrizi L, Nigro L, Cappella F, Spagnoli F, Guirguis M, Niveau de Villadry y Mariñas AM, Doménech-Carbó MT, Doménech-Carbó A (2020) Discrimination and provenances of Phoenician red slip ware using both the solid state electrochemistry and petrographic analyses. Electroanalysis 32:258–270
12. Doménech-Carbó A, Giannuzzi M, Mangone A, Giannossa LC (2022) Electrochemical methods to discriminate technology and provenance of Apulian red-figured pottery. I VIMP and SECM Archaeometry 64:1325–1339
13. Peter LM (2013) Energetics and kinetics of light-driven oxygen evolution at semiconductor electrodes: the example of hematite. J Solid State Electrochem 17:315–326
14. Zhu H, Zhang S, Huang YX et al (2013) Monodisperse MxFe3-xO4 (M = Fe, Cu Co, Mn) nanoparticles and their electrocatalysis for oxygen reduction reaction. Nano Lett 13:2947–2951
15. Shimizu K, Tschulik K, Compton RG (2016) Exploring the mineral-water interface: reduction and reaction kinetics of single hematite ($\alpha$-$Fe_2O_3$) nanoparticles. Chem Sci 7:1408–1414
16. Shimizu K, Sepunaru L, Compton RG (2016) Innovative catalyst design for the oxygen reduction reaction for fuel cells. Chem Sci 7:3364–3369
17. Bouhjar F, Bessaïs B, Marí B (2018) Ultrathin-layer $\alpha$-$Fe_2O_3$ deposited under hematite for solar water splitting. J Solid State Electrochem 22:2347–2356
18. Wan H, Lv M, Liu X, Chen G, Zhang N, Cao Y, Wang H, Ma R, Qiu G (2019) Activating hematite nanoplates via partial reduction for electrocatalytic oxygen reduction reaction. ACS Sustain Chem Eng 7:11841–11849
19. Doménech-Carbó A (2022) Description of solid-to-solid redox processes based on the voltammetry of immobilized particles methodology: a logistic approximation. J Phys Chem C 126:11822–11832
20. Doménech-Carbó Antonio (2024) Exploring nucleation modeling of the voltammetry of solid-to-solid-state redox processes with phase changes. J Solid State Electrochem 28:1497–1507. https://doi.org/10.1007/s10008-023-05572-0
21. Doménech-Carbó A, López S, Muñoz E (2024) Logistic approximation to ion-intercalation electrochemistry: application to potassium−copper(II) hexacyanoferrate in DMSO electrolytes. J Phys Chem C 128:1487–1495
22. Gavilán-Arriazu EM, Barraco DE, Leiva EPM (2021) On how interactions influence kinetic limitations in alkali-ion batteries. Application to Li-ion intercalation into graphite through voltammetric experiments. J Solid State Electrochem 25:2793–2806
23. Gavilán-Arriazu EM, Mercer MP, Barraco DE, Hoster HE, Leiva EPM (2022) Voltammetric behaviour of LMO at the nanoscale: a map of reversibility and diffusional limitations. ChemPhysChem 23:e202100700
24. De Vito C, Medeghini L, Mignardi S, Orlandi D, Nigro L, Spagnoli F, Lottici PP, Bersani D (2014) Technological fingerprints of Black-Gloss Ware from Motya (Western Sicily, Italy). Applied Clay Science, volumes 88–89:202–213
25. Medeghini L, Mignardi S, Di Fusco G, Botticell M, Coletti F, De Vito C (2020) How microanalysis can be discriminant on black Pompeian wares. Crystals 10:879. https://doi.org/10.3390/cryst10100879
26. Coletti F, Prascina C, Sterpa G, Witte N (2010) Venus Pompeiana. Scelte progettuali e procedimenti tecnici per la realizzazione di un edificio sacro tra tarda repubblica e primo impero. In: Camporeale S, Dessales H, Pizzo A (eds) ArquelogÌa de la Construcción, II. pp 198–211
27. Coletti F (2020) Ceramica a vernice nera a Pompei. Il caso dei depositi votivi del santuario die Venere Fisica: produzione, circolazione e mercati. Un primo bilancio. In: Osanna M, Tonionlo L (eds) Fecisti Cretaria. Dal frammento al contesto: studi sul vasellame ceramico dal territorio vesuviano, 1st ed. pp 77–95
28. Curti E (2008) La Venere Fisica trionfante. Un nuovo ciclo di iscrizioni dal tempio di Venere a Pompei. In: Masseria C (ed) Il filo e le perle. A Mario Torelli per i suoi settant'anni, 1st ed. Venosa, pp 67–81

29. Curti E (2007) Il tempio di venere Fisica e il porto di Pompei. In: Guzzo PG, Guidobaldi MP (eds) Nuove ricerche archeologiche nell'area vesuviana (scavi 2003–2006). Studi della Soprintendenza Archeologica di Pompei, Roma, pp 47–59
30. Curti E (2005) Le aree portuali di Pompei: ipotesi di lavoro. In: Scarani Ussano V (ed) Moregine. Suburbio portuale di Pompei, 1st ed. pp 51–76
31. Whitbread I, Mari A (2014) Provenance and proximity: a technological analysis of Late and Final Neolithic ceramics from Euripides Cave, Salamis, Greece. J Archaeol Sci 41:79–88. https://doi.org/10.1016/j.jas.2013.07.020
32. Whitbread IK (1986) The characterisation of argillaceous inclusions in ceramic thin sections. Archaeometry 28:79–88. https://doi.org/10.1111/J.1475-4754.1986.TB00376
33. Doménech-Carbó A, Giannuzzi M, Mangone A, Giannossa LC, Di Turo F, Cofini E, Doménech-Carbó MT (2022) Hematite as an electrocatalytic marker for the study of archaeological ceramic clay bodies: a VIMP and SECM study. ChemElectroChem 9:e202101197
34. Levi MD, Aurbach D (1997) The mechanism of lithium intercalation in graphite film electrodes in aprotic media. Part 1. High resolution slow scan rate cyclic voltammetric studies and modeling. J Electroanal Chem 421:79–88
35. Levi MD, Aurbach D (1999) Frumkin intercalation isotherm — a tool for the description of lithium insertion into host materials: a review. Electrochim Acta 45:167–185
36. Richards FJ (1959) A flexible growth function for empirical use. J Exp Bot 10:290–301
37. Meyer PS, Yung JW, Ausubel JH (1999) A primer on logistic growth and substitution: the mathematics of the Loglet Lab software. Technol Forecast Soc Change 61:247–271
38. Wilson EB (1925) The logistic or autocatalytic grid. Proc Nat Acad Sci USA 11:451–456
39. Gavilán-Arriazu EM, Barraco DE, Ein-Eli Y, Leiva EPM (2022) Fast charging of alkali-ion batteries at the single-particle level: the impact of particle geometry on diffusional and kinetic bottlenecks in voltammetry. J Solid State Electrochem 26:1995–2003
40. Meyer P (1994) Bi-logistic growth. Technol Forecast. Soc Change 47:89–102
41. Volterra V (1931) Leçons sur la Théorie Mathématique de la Lutte pour la Vie. Jacques Gabay, Paris
42. Gilpin ME, Ayala FJ (1973) Global models of growth and competition (population dynamics/niche theory/coexistence). Proc Nat Acad Sci USA 70:3590–3593
43. Malaie K, Scholz F, Schröder U (2023) A thermodynamic model for the insertion electrochemistry of battery cathodes. ChemElectroChem 10:e202201118
44. Malaie K, Scholz F, Schröder U, Wulff H, Kahlert H (2022) Determining the Gibbs energy contributions of ion and electron transfer for proton insertion in ϵ-$MnO_2$. ChemPhysChem 23:e202200364
45. Klahr B, Hamann T (2014) Water oxidation on hematite photoelectrodes: insight into the nature of surface states through in situ spectroelectrochemistry. J Phys Chem C 118:10393–10399
46. Cummings CY, Marken F, Peter LM, Tahir AA, Ugul Tijayantha KG (2012) Kinetics and mechanism of light-driven oxygen evolution at thin film α-$Fe_2O_3$ electrodes. Chem Commun 48:2027–2029
47. Cummings CY, Marken F, Peter LM, Ugul Tijayantha KG, Tahir AA (2012) New insights into water splitting at mesoporous α-$Fe_2O_3$ films: a study by modulated transmittance and impedance spectroscopies. J Am Chem Soc 134:1228–1234
48. Le Formal F, Pastor E, Tilley SD, Mesa CA, Pendlebury SR, Grätze M, Durrant JR (2015) Rate law analysis of water oxidation on a hematite surface. J Am Chem Soc 137:6629–6637
49. Zhao Q, Yan Z, Chen C, Chen J (2017) Spinels: controlled preparation, oxygen reduction/evolution reaction application, and beyond. Chem Rev 117:10121–10211
50. Zhang Y-Q, Liao R-Z (2017) Reaction mechanism of hydrogen evolution catalysed by Co and Fe complexes containing a tetradentate phosphine ligand-a DFT study. Phys Chem Chem Phys 19:32589–32596
51. Dolganov AV, Belaya IG, Voloshin YZ (2014) Binuclear iron(II) cage complexes as electrocatalysts of hydrogen evolution reaction in different hydrogen-producing systems. Electrochim Acta 125:302–306
52. Rana A, Mondal B, Sen P, Dey S, Dey A (2017) Activating Fe(I) Porphyrins for the hydrogen evolution reaction using second-sphere proton transfer residues. Inorg Chem 56:1783–1793